Determination of size distributions of non-spherical pores or particles from single x-ray phase contrast images

A. F. T. Leong,[1,3] E. Asare,[2] R. Rex,[2] X. H. Xiao,[4] K. T. Ramesh,[1,2,3] and T. C. Hufnagel[1,3,*]

[1]*Department of Material Science and Engineering, Johns Hopkins University, 3400 North Charles St., Baltimore, MD, 21218, USA*
[2]*Department of Mechanical Engineering, Johns Hopkins University, 3400 North Charles St., Baltimore, MD, 21218, USA*
[3]*Hopkins Extreme Materials Institute, Johns Hopkins University, 3400 North Charles St., Baltimore, MD, 21218, USA*
[4]*Sector 2, Advanced Photon Source, Argonne National Laboratory, 9700 Cass Ave., Lemont, IL, 60439, USA*
[*]*hufnagel@jhu.edu*

Abstract: Although x-ray tomography is commonly used to characterize the three-dimensional structure of materials, sometimes this is impractical due either to limited time for data collection (such as in rapidly-evolving systems) or the need to limit the radiation exposure of the sample. In such situations, it is desirable to extract as much information as possible from a more limited data set. In this paper, we describe how to extract the size distribution of non-spherical pores (or, equivalently, particles) from single x-ray phase contrast imaging (XPCI). Because the pores overlap in projection, interpreting the images and extracting quantitative information about the size distribution is non-trivial. In this paper we extend a previously-developed Fourier-based framework for interpreting the speckle pattern of XPCI images from materials with spherical pores to the more challenging case of non-spherical pores. We develop an analytical expression for the XPCI image from a distribution of randomly-oriented ellipsoidal pores, and show that we can use this expression to extract quantitative information about the size distribution from single images. We discuss three approaches to evaluating this expression, corresponding to different assumptions about the nature of the size distribution, and validate our results with simulated XPCI images and experimental data from Berea sandstone.

1. Introduction

Several experimental techniques can be used to measure pore or particle size distributions in materials. Some, such as x-ray computed tomography [1], magnetic resonance imaging [2], and positron emission tomography [3] provide rich three-dimensional (3D) structural information from which the size distribution can be extracted.

There are situations, however, in which one would like to measure pore or particle size distributions dynamically in a rapidly-evolving system; examples include granular flow [4], particle droplets in fuel injectors [5], cosmetic emulsifying systems [6], and alveolar recruitment in animals [7]. If, in such situations, the structure evolves too rapidly to allow collection of 3D structural information from tomographic techniques, it would be desirable to obtain as much information as possible from single, two-dimensional (2D) projected images through the specimen.

The penetrating power of x-rays, together with the availability of high-brilliance sources, makes them ideally suited for this purpose. In addition, modern synchrotron x-ray sources provide partial spatial coherence, enabling x-ray phase contrast imaging (XPCI) for improved

resolution of pore (or particle) boundaries and providing additional information (over attenuation contrast) about the 3D structure of materials [8].

In this work, we describe a technique for extracting information about 3D size distributions for micron-scale features from single 2D XPCI images, with sub-microsecond temporal resolution. Our approach has utility beyond dynamic studies, however; in a clinical context, for example, the ability to extract 3D information from single images could be useful for diagnostic examination of porous structures (such as lungs and bones) with reduced radiation exposure for the patients, as compared to conventional x-ray computed tomography [9, 10].

2. Background

The literature on characterization of porous and particulate systems is extensive. The details of the techniques employed to measure pore (or particle) size distributions depend on the system of interest. Broadly speaking, however, we can classify the relevant techniques as based on physical properties, scattering or imaging.

Beginning with measurements based on physical properties, mercury intrusion porosimetry and nitrogen adsorption-desorption [11–13] are commonly used to characterize porous materials. These techniques are relatively slow and they necessarily average over the entire sample volume. This makes them of little use in studying dynamic systems, and we do not consider them further.

Small-angle x-ray scattering (SAXS) and small-angle neutron scattering (SANS) have long been used to study pore and particle sizes in a variety of important materials [14]. Typical feature sizes studied by SAXS and SANS are less than 100 nm, although specialized instruments capable of ultra-SAXS and ultra-SANS can measure features as large as 1 μm [15], and larger features can be observed in ultra-SAXS imaging mode [16]. However, none of these techniques have sufficient temporal resolution to permit dynamic studies of particulate systems.

Turning to imaging, transparent materials can be examined by optical techniques, including confocal microscopy for small particles [17] and refractive index matched scanning [18] for larger particles. Because these are scanning techniques, however, they are limited to studies of static or slowly-evolving systems. Opaque specimens can be studied by x-ray computed tomography, but again the relatively low scan speeds (seconds to hours) limit the applications of this technique for dynamic studies.

Recently, several groups have attempted to obtain quantitative information about particulate or porous materials from single 2D x-ray images, which should enable studies of rapidly-evolving systems. For example, Guillard and coworkers employed radiography to measure the size and orientation of micron-scale grains and glass beads using a Fourier-based approach [19], but this technique gives only relative measures of single size pores. Cerbino and coworkers [20] discussed the possibility of extracting time-resolved structural information about particulate systems from their near-field speckle patterns produced in XPCI. Carnibella and coworkers [21, 22] extracted particle size distributions from XPCI data by iteratively fitting spatial autocorrelation functions (SAFs) from simulated XPCI images to experimental data. One drawback to this approach is that the experimental XPCI images are divided into subregions, from which the SAFs are calculated and averaged. This is problematic for dynamic studies when the size distributions are spatially heterogeneous. Finally, Leong *et al.* [23] developed a mathematical model to relate the power spectrum of a single 2D XPCI image to the total pore number and mean pore radius, but the model was limited to spherical pores and no attempt was made to determine the complete pore size distribution (PSD).

To summarize, most current techniques for measuring PSD are restricted to static or slowly-evolving systems, or have other limitations (such as being restricted to transparent materials). The few imaging and analysis techniques that can measure PSD dynamically also have limitations, such as the assumption of spherical features. In this work, we extend the mathematical model developed by Leong *et al.* [23] to a more general ellipsoidal pore shape and show how to extract

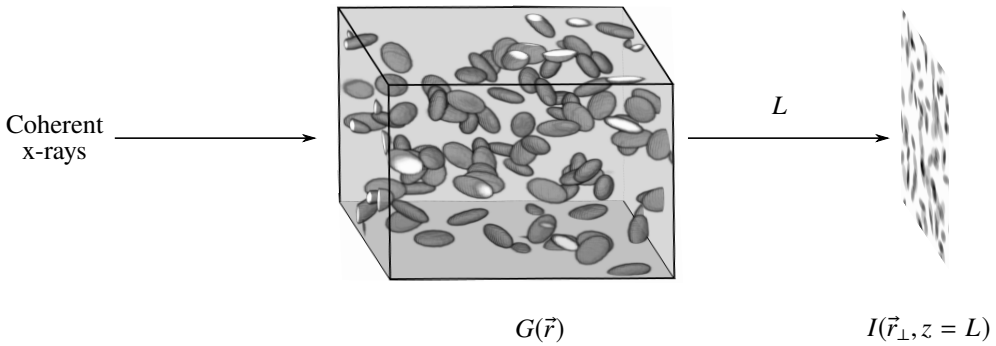

Fig. 1. Schematic of the experimental setup for XPCI imaging of a porous/colloidal object, modelled as ellipsoidal-shaped pores/particles embedded in a homogeneous single material.

PSD from a single 2D XPCI image under the assumption that the pores are randomly oriented and spatially distributed. We lay out the theoretical groundwork in section 3 where an implicit analytical expression as a function of the PSD and its 2D XPCI image is derived. In section 4 we describe three approaches to solving this expression for different limiting cases, and demonstrate the three approaches using simulated and experimental XPCI images of Berea sandstone. Finally, in section 5 we compare the results of the three approaches and discuss the applicability of each.

3. Theory

To calculate the ellipsoidal PSD from a single 2D XPCI image (see Fig. 1), we begin with an expression (derived by Leong and coworkers [23]) that relates the projected thickness $G_z(\vec{r}_\perp)$ of an object to the intensity of its 2D XPCI image $I(\vec{r}_\perp, z = L)$:

$$\left|\mathcal{F}\left\{\frac{I(\vec{r}_\perp, z = L)}{I(\vec{r}_\perp, z = 0)} - 1\right\}\right|^2 = L^2\delta^2\left|\vec{k}_\perp\right|^4 \left|\mathcal{F}\left\{G_z(\vec{r}_\perp)\right\}\right|^2, \tag{1}$$

where the thickness is projected along the x-ray beam propagation direction z. On the left hand-side of this expression, the image intensity recorded at propagation distance (sample-to-detector) L is normalized to the intensity at $z = 0$, which corresponds to the attenuation intensity (*i.e.*, without phase contrast). $\mathcal{F}$ denotes the Fourier transformation with respect to $\vec{r}_\perp = (x, y)$. $\vec{k}_\perp = (k_x, k_y)$ is a vector in Fourier space perpendicular to z, with k_x and k_y being its components along x and y, respectively. We refer to the left-hand side of Eq. 1 as the XPCI power spectrum. On the right-hand side, δ is the refractive index decrement of either the particles in a particulate system or material surrounding the pores in a single material porous object. In the proceeding derivation, we assume a porous object but the same derivation can be made for a size distribution of particles.

Equation 1 assumes a monochromatic, spatially coherent x-ray beam. In addition, the object is assumed to be both weakly absorbing (*i.e.*, $\mu\Delta G_z(\vec{r}_\perp) < 1$, where μ is the attenuation coefficient corresponding to the same material as δ) and weakly scattering (*i.e.*, $\frac{a_L}{L\lambda|\nabla_\perp\phi|_{\max}} > 1$, where a_L is the characteristic pore length scale, λ is the x-ray wavelength and $|\nabla_\perp\phi|_{\max}$ is the maximum x-ray wavefield phase gradient transverse to the direction of propagation). These conditions can be satisfied by recording XPCI images at sufficiently small L and/or high x-ray energy [24].

To develop our model, we use Eq. 1 to calculate the power spectrum of an object with embedded ellipsoidal-shaped pores. An individual pore in an arbitrary orientation can be represented by its

shape function,

$$E(\vec{r}) = \begin{cases} 1 & \text{if } \frac{x'^2}{a^2} + \frac{y'^2}{b^2} + \frac{z'^2}{c^2} \leq 1, \\ 0 & \text{otherwise.} \end{cases} \tag{2}$$

The semi-axes of the ellipsoid are a, b, and c. The orientation of the ellipsoid is defined by a new coordinate system, rotated from the original by Euler angles Φ, Θ and Γ around x, y and z, respectively, and x', y', and z' are coordinates of $\vec{r}$ in this new system.

For ease in computation we assume that the distribution of pore sizes is uniformly discretized with each bin specified by an index i and the semi-axes of the ellipsoids in this bin being a_i, b_i, and c_i. There can be more than one pore of each size, so n_i^{el} refers to the number of ellipsoidal pores in the ith bin. The total number of pores is therefore $N^{el} = \sum_{i=1}^{B} n_i^{el}$ where B is the number of discrete bins.

We can now describe our material model in terms of the pore shape function

$$G(\vec{r}) = V(\vec{r}) - \sum_{i=1}^{B} \sum_{j=1}^{n_i^{el}} \hat{\delta}(\vec{r} - \vec{r}_{ij}) * E_i(\vec{r}), \tag{3}$$

where $\vec{r}_{ij}$ denotes the position of the jth pore in the ith bin. $V(\vec{r})$ is unity within the bounds of the material and zero outside, $\hat{\delta}$ is the Dirac delta function, and $*$ is the convolution operator.

To calculate $|\mathcal{F}\{G(\vec{r})\}|^2$ we assume that the pores are randomly distributed in the object. The power spectrum of Eq. 3 is then [25]:

$$|\mathcal{F}\{G(\vec{r})\}|^2 = \sum_{i=1}^{B} n_i^{el} |\mathcal{F}\{E_i(\vec{r})\}|^2, \tag{4}$$

for $k = \left|\vec{k}\right| \geq \epsilon > 0$, where ϵ is a real constant and the power spectrum $E(\vec{r})$ of an ellipsoid in spherical coordinates is given by

$$|\mathcal{F}\{E_i(\vec{r})\}|^2 (k, \theta_q, \phi_p) = \left| \frac{v_i^{el}}{\left(\left(R_i(\theta_p, \phi_q)\right) k\right)^2} \left[\frac{\sin\left(R_i\left(\theta_q, \phi_p\right) k\right)}{R_i(\theta_q, \phi_p) k} - \cos\left(R_i\left(\theta_q, \phi_p\right) k\right) \right] \right|^2, \tag{5}$$

and where

$$R_i(\theta_q, \phi_p) = \sqrt{(a_i \cos\theta_q \sin\phi_p)^2 + (b_i \sin\theta_q \sin\phi_p)^2 + (c_i \cos\phi_p)^2}, \tag{6}$$

can be interpreted as the ellipsoid radius defined from the ellipsoid center of symmetry in the direction $(\theta_q, \phi_p) = (\frac{q\pi}{Q}, \frac{p2\pi}{P})$ with $q \in \mathbb{N} \cap [1, Q]$ and $p \in \mathbb{N} \cap [1, P]$. We define θ to be the azimuthal angle in the $k'_x k'_y$-plane from the positive k'_x-axis and ϕ to be the polar angle from the positive k'_z-axis. (k'_x, k'_y, k'_z) are the rotated coordinates corresponding to (x', y', z'). Q and P represent the number of times θ and ϕ are sampled, respectively. $v_i^{el} = \frac{4}{3}\pi a_i b_i c_i$ is the volume of the ellipsoid in the i^{th} bin size. The shape function $V(\vec{r})$ also contributes to the XPCI power spectrum. However, if its size is sufficiently large relative to the largest ellipsoid, then its contribution is significant only for $k < \epsilon$.

We make a further assumption that the ellipsoids are randomly oriented. Dropping the explicit dependence on θ_q and ϕ_p in R_i for notational simplicity, the power spectrum of a random orientation and spatial distribution of ellipsoids reduces to a one-dimensional (1D) function of k, that is:

$$|\mathcal{F}\{G(\vec{r})\}|^2 = \frac{1}{4\pi} \sum_{i=1}^{B} n_i^{el} \sum_{p=1}^{P} \sum_{q=1}^{Q} \sin\phi_p \left| \frac{v_i^{el}}{(R_i k)^2} \left[\frac{\sin(R_i k)}{R_i k} - \cos(R_i k) \right] \right|^2. \tag{7}$$

Substituting Eq. 7 into Eq. 1 gives the XPCI power spectrum of randomly oriented and spatially distributed ellipsoids:

$$\left|\mathcal{F}\left\{\frac{I(\vec{r}_\perp, z=L)}{I(\vec{r}_\perp, z=0)}-1\right\}\right|^2 = \frac{L^2\delta^2k^4}{4\pi}\sum_{i=1}^{B} n_i^{el}\sum_{p=1}^{P}\sum_{q=1}^{Q}\sin\phi_p\left|\frac{v_i^{el}}{(R_ik)^2}\left[\frac{\sin(R_ik)}{R_ik}-\cos(R_ik)\right]\right|^2. \quad (8)$$

For the forward modeling case, Eq. 8 can be used to calculate the XPCI power spectrum from a known PSD (under the assumptions specified above). More commonly, we would like to use Eq. 8 to determine characteristics of an unknown PSD from the measured XPCI power spectrum. In the next section we discuss and show examples of three approaches to this problem.

4. Methodology and results

In Eq. 8 for the XPCI power spectrum there are four independent variables (a_i, b_i, c_i, and n_i^{el}) for each of the B bins in the ellipsoid size distribution, for a total of $4B$ independent variables. The number of independent equations we have to solve for these variables is defined as M, which is the number of different k values in which the XPCI power spectrum is sampled.

The best way to determine the characteristics of an unknown pore (or particle) size distribution from the measured XPCI data depends on the ratio of the number of unknowns to independent equations, and whether the unknowns are themselves mutually independent. We therefore present three approaches to the solution of Eq. 8, corresponding to these three cases:

1. $M \geq 4B$: If the number of independent measurements M equals the number of unknowns $4B$, then Eq. 8 has a unique solution for each of the unknowns. If $M > 4B$ the equation is overdetermined and a solution can be obtained by least-squares fitting.

The condition $M \geq 4B$ implies a severely restricted number of bins in the size distribution. This is conceivable in situations where the pore or particle sizes are constrained (a dispersion of identical colloidal particles, for example). More commonly there is a wide distribution of sizes and consequently $M < 4B$, in which case the system of equations required to solve for the size distribution is under-determined and no unique solution exists. We present two approaches to this situation:

2. $M < 4B$ *and the PSD can be approximated by a function* $n^{el}(a, b, c)$: In many cases of practical interest it will be possible to describe the PSD by an analytical function $n^{el}(a, b, c)$ with parameters p_i. The number of parameters becomes the number of independent variables that needs to be solved (instead of $4B$), which is much less than M. This allows the parameters and hence the analytical approximation of the PSD to be determined by least-squares minimization.

3. $M < 4B$ *but the PSD cannot be approximated by a function* $n^{el}(a, b, c)$: This is the most difficult case, and applies to situations where the PSD is either sparse or non-uniform so that it cannot be approximated by an analytical function. Although a direct solution for the ellipsoidal PSD is then not possible, we can still obtain important information about the structure of the material by making additional approximations, as described in section 4.1.3.

These cases assume that the M equations are independent of each other, which may not always hold true depending on the domain of solutions considered. This is difficult to address theoretically and is compounded by image noise, so we investigate the stability and accuracy of Eq. 8 for each of the three cases by testing them on simulated noisy XPCI data from sandstone, as described in the following sections. We conclude this part of the paper by extracting information about the PSD from experimental XPCI images of sandstone, using the third approach.

4.1. Simulated sandstone

To demonstrate the three approaches to solving Eq. 8, XPCI images of sandstone are simulated with conditions similar to our experimental studies of Berea sandstone (described in section 4.2 below). The imaging conditions are summarized in Table 1.

Table 1. Parameters used for simulating XPCI images of sandstone.

X-ray energy (keV)	20.4
Pixel size (μm)	3.25
Source-to-sample distance (m)	∞
Sample-to-detector distance, L (m)	0.1
Attenuation coefficient, μ (m^{-1})	611
Refractive index decrement, δ	1.3×10^{-6}

To create a material model $G(\vec{r})$ of sandstone for XPCI simulations, we begin with a $2.2 \times 2.2 \times 3.25$ mm^3 material $V(\vec{r})$ with attenuation coefficient μ and refractive index decrement δ (Table 1), and place in it randomly distributed and randomly oriented ellipsoidal-shaped voids drawn from a chosen PSD. μ is measured experimentally and is described in section 4.2, while δ corresponds to that of quartz and is obtained from XOP [26]. The spatial coordinates $\vec{r}_{ij}$ of each ellipsoid are randomly generated using the Mersenne Twister uniform pseudo-random number generator algorithm [27]. The orientation (Φ, Θ, Γ) of each ellipsoid is generated from three uniformly-distributed random numbers $u_1, u_2, u_3 \in [0, 1]$ (again using the Mersenne Twister algorithm) to compute a uniform, random unit quarternian [28]:

$$h = \left[\sqrt{1-u_1}\sin(2\pi u_2),\ \sqrt{1-u_1}\cos(2\pi u_2), \sqrt{u_1}\sin(2\pi u_3),\ \sqrt{u_1}\cos(2\pi u_3)\right], \tag{9}$$

which is converted into Euler angles to rotate the ellipsoid.

The porous material model $G(\vec{r})$ is projected along the x-ray beam propagation direction (z) to calculate its projected thickness image $G_z(\vec{r}_\perp)$, from which its XPCI image is simulated using the angular spectrum method of scalar wave optics [29]:

$$I(\vec{r}_\perp, z = L) = \left|\mathcal{F}^{-1}\left\{P(\vec{k}_\perp, z = L)\mathcal{F}\left\{\psi(\vec{r}_\perp, z = 0)\right\}\right\}\right|^2. \tag{10}$$

Here, $\psi(\vec{r}_\perp, z = 0) = \sqrt{I(\vec{r}_\perp, z = 0)}\exp(i\phi(\vec{r}_\perp, z = 0))$ is the exit surface wavefield of the material, where $I(\vec{r}_\perp, z = 0)$ and $\phi(\vec{r}_\perp, z = 0)$ are computed from $G_z(\vec{r}_\perp)$ using the projection approximation [30]. The attenuation coefficient μ and refractive index decrement δ are inputs in the projection approximation. $P(\vec{k}_\perp, z = L)$ is the wave propagator and $\mathcal{F}^{-1}$ is the inverse 2D Fourier transform with respect to $\vec{k}_\perp$. To ensure numerical accuracy of the simulated XPCI images, it is important to choose a sufficiently small pixel size (Δx) such that both the exit wave function $\psi(\vec{r}_\perp, z = 0)$ and the wave propagator $P(\vec{k}_\perp, z = L)$ are adequately sampled. According to the Nyquist-Shannon sampling theorem, adequate sampling of $\psi(\vec{r}_\perp, z = 0)$ requires $\Delta x \geq \frac{1}{2k_N}$, where k_N is the spatial frequency bandwidith. Although XPCI images of porous materials are generally not spatial frequency bandlimited (*i.e.*, k_N is not finite), in practice there is a spatial frequency cutoff k_N above which the spectral density signal-to-noise ratio is < 1 due to the effects of image noise, detector point spread function (PSF), and partially coherent X-ray source. Therefore, the XPCI images need only be accurately simulated for spatial frequencies $k \leq k_N$. We determine k_N experimentally for our conditions by imaging and computing the XPCI power

spectrum of a region of a specimen of uniform thickness, and average over a range of spatial frequencies to obtain the average image noise spectral density. For the porous materials simulated here, we find that the spectral density falls below the image noise at $k_N \approx 35.1$ mm^{-1}, which we therefore take as the bandwidth limit for our simulations.

Although the pixel size must satisfy $\Delta x \geq \frac{1}{2k_N}$ for $\psi(\vec{r}_\perp, z = 0)$ to be adequately sampled, $\psi(\vec{r}_\perp, z = 0)$ is constructed from a product of two functions, an intensity map image $I(\vec{r}_\perp, z = 0)$ and a phase map image $\phi(\vec{r}_\perp, z = 0)$, the sampling of which we consider separately. $I(\vec{r}_\perp, z = 0)$ needs to be sampled with pixel size $\Delta x \geq \frac{1}{4k_N}$ in order to adequately sample $\psi(\vec{r}_\perp, z = 0)$ at $\Delta x \geq \frac{1}{2k_N}$ [31]. Applying this to $k_N \approx 35.1$ mm^{-1}, the maximum allowable pixel size is 3.5 μm. For $\phi(\vec{r}_\perp, z = 0)$, the pixel size set must be such that the phase map image gradient is less than $\pi/2$ radians per pixel across every pixel. We found through trial of a range of pixel sizes to simulate Berea sandstone samples that a size on the order of 10^{-8} m is needed to adequately sample $\phi(\vec{r}_\perp, z = 0)$. Choosing this small size means an extremely large array is required to calculate XPCI models with a sufficient number of voids to satisfy our assumptions of random spatial distribution and orientation, rendering the simulations impractical. To make the simulations tractable, we chose a pixel size of 3.25 μm, which adequately samples $I(\vec{r}_\perp, z = 0)$ and matches the pixel size of our experimental XPCI images of Berea sandstone. To compensate for the fact that this pixel size does not adequately sample $\phi(\vec{r}_\perp, z = 0)$, we artificially reduce the refractive index decrement δ by a factor of 1000 to ensure that the maximum phase map gradient is $\leq \pi/2$ before simulating the XPCI power spectrum. The factor of 1000 is multiplied back in to correctly return the XPCI power spectrum corresponding to δ. In general, δ is a non-linear term in Eq. 10. However, under the assumption of a weakly scattering and absorbing specimen, Eq. 10 reduces to Eq. 1 (see [29]) where δ becomes a multiplicative factor. Therefore, in this case the angular spectrum method yields XPCI images that depend on δ by a multiplicative factor.

The effects of imaging PSF and noise are incorporated into simulated XPCI power spectra. To show how these are handled, we describe the overall process for simulating a XPCI power spectrum:

1. Equation 10 is used to generate an XPCI image of a material model $G(\vec{r})$. The 'reduced' δ is used, which corresponds to that given in Table 1 before being reduced by a factor of 1000;

2. The simulated XPCI image is divided by its attenuation image, which is calculated using the single image phase retrieval algorithm [30] and the reduced δ;

3. The resultant image is subtracted by unity and multiplied by 1000. Then, unity is added back to the image and multiplied by the attenuation image calculated in step 2. This returns the XPCI image equivalent to that of an image directly simulated using δ in Eq. 10 if the sample is weakly scattering and absorbing;

4. The Fourier transform of the image is multiplied with an azimuthally symmetric Pearson type VII distribution function (P_F) [32],

$$P_F(k) = p_0 \left[1 + \frac{(k - p_1)^2}{p_2 p_3^2} \right]^{-p_2}, \tag{11}$$

with parameters $p_0 = 0.0086$, $p_1 = 7.32 \times 10^{-6}$, $p_2 = 0.57$ and $p_3 = 0.059$, to account for the detector PSF and partially coherent x-ray source. These parameters are determined using an experimentally-recorded XPCI image of a sharp edge under the experimental conditions given in Table 1. Ideally the image should be recorded at $z = 0$ to avoid being contaminated with phase contrast. However, we found that such contamination (in the form of Fresnel fringes from the sharp edge) at the chosen propagation distance was negligible.

5. Gaussian noise (N_I) with standard deviation of 0.1 is added to the convolved image to give an SNR≤10 (SNR=10 corresponding to a transparent material). This upper limit is determined from the SNR measured of a single crystal quartz with uniform thickness approximately equal to the average of that of quartz in the Berea sandstone samples.

6. Finally, the image is divided by its attenuation image calculated using the single image phase retrieval algorithm [30] with δ.

To account for the imaging PSF and noise when solving for the PSD, Eq. 8 is generalized to [Eq. 8]$\times P_F^2 + |\mathcal{F}\{N_I\}|^2$. The parameters of the imaging PSF and noise are the same as those in the simulation of the XPCI power spectra. Note though, image noise is independently generated for simulating the XPCI power spectra and solving for the PSD.

4.1.1. Case 1 ($M \geq 4B$)

If $M \geq 4B$ then there exists at least one least squares solution for each unknown $(a_i, b_i, c_i, n_i^{el})$ in Eq. 8. Except when $M = 4B$, Eq. 8 is an overdetermined system of non-linear equations and we can use the Levenberg-Marquardt least squares method to solve for the PSD [33]. To test this approach, we create a model porous material having two different pore sizes, the parameters of which are given in Table 2. We directly simulate the XPCI image of 100 instantiations of such a material, with the voids randomly spatially distributed and oriented in the material as described above, and calculate their XPCI power spectra. The result for one of the instantiations is shown as the blue solid line in Fig. 2(a). The XPCI power spectrum from our model, Eq. 8, is calculated starting with initial guesses of the parameters, and fitted to the simulated data using the Levenberg-Marquardt algorithm. The result of the fit is shown as the red dashed line in Fig. 2(a). The initial guesses of the parameters are not randomly chosen but determined through assuming the calculated XPCI power spectrum is a representation of spherical voids. Then using the algorithm developed by Leong *et al.* [34], the total population of spheres calculated is divided equally into n_1 and n_2 and the mean sphere radius is assigned to a_1, b_1, c_1, a_2, b_2 and c_2 (Table 2).

The fitted parameters show good agreement with pore size 2 but significantly less so for pore size 1. This is due in part to image noise. Despite our algorithm accounting for image noise as an additional term in the XPCI power spectrum, in the simulated XPCI power spectrum noise is incorporated in the XPCI image. This implicitly assumes that there is zero correlation between noise and sample image, which is not true because the degree of noise is dependant on the projected sample thickness. Another contributing factor is that the assumption of a weakly-absorbing material may not be entirely satisfied even though $\mu\Delta G_z(\vec{r_\perp}) < 0.1$. It is difficult to predict, in general, how these errors affect the fitted parameters since they probably depend on the specific PSD. Despite these factors, for this particular example the overall aspect ratios of the ellipsoids are captured. Suggestions for further improvements are provided in Section 5.

4.1.2. Case 2 ($M<4B$ & $n^{el}(a,b,c)$ exists)

When $M < 4B$ the system of non-linear equations from Eq. 8 is under-determined and a unique solution for PSD does not exist. However, if the PSD can be described by an analytical function $n^{el}(a, b, c)$ then the number of unknowns to solve is reduced to that of parameters in the function, the values of which can be found using a least-squares approach as in Case 1.

As an example, we simulate 20 instantiations of a XPCI image for a material with a PSD given by

$$n^{el} = \frac{650}{\sqrt{h_0 a + h_1 b^{1.5} + h_2 c^2}}. \tag{12}$$

The results of fitting of this model with three parameters h_i $(i = 0, 1, 2)$ to the simulated XPCI power spectrum are shown in Fig. 2(b) and Table 3 using the Levenberg-Marquardt least squares

Table 2. PSD parameters (pore size in μm) and results of fit for Case 1 ($M \geq 4B$). The initial guess and fit result are represented by nominal (range) values across the instantiations.

	Pore size 1				Pore size 2			
	n_1	a_1	b_1	c_1	n_2	a_2	b_2	c_2
Model	2000	16.3	32.5	48.8	2000	48.8	48.8	48.8
Initial guess	852 (±48)	50.7 (±0.7)	50.7 (±0.7)	50.7 (±0.7)	852 (±48)	50.7 (±0.7)	50.7 (±0.7)	50.7 (±0.7)
Fit result	1239 (±562)	16.6 (±3.9)	64.4 (±10.6)	75.7 (±26.3)	2075 (±105)	48.8 (±1.0)	49.1 (±2.0)	48.8 (±1.0)

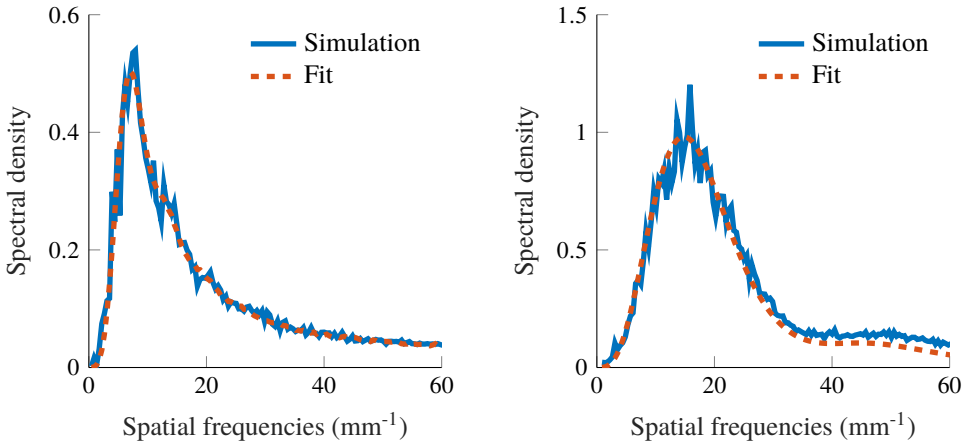

Fig. 2. Comparison of simulated XPCI power spectra (solid blue line) with fits to model (dashed red line) for (a) Case 1 ($M \geq 4B$), a PSD with a small number of discrete pore shapes, and (b) Case 2 ($M < 4B$), a PSD that can be described by an analytical function.

method. Like case 1, the initial guesses for the parameters are calculated based on Leong *et al.* [34]. In this case, the mean sphere size is made to represent the median ellipsoid size of the PSD. To determine the corresponding h_i, we approximate Eq. 12 as one-dimensional, given by, $n^{el} = \frac{650}{h_{1D} d^{0.75}}$, where d is the ellipsoid size. The corresponding h_{1D} is then calculated and assigned to the initial guesses of each of the three parameters h_i.

In this approach, the XPCI power spectrum of each of the B ellipsoid size bins needs to be simulated and summed to calculate the XPCI power spectrum of the material model at each iteration. However, to adequately sample the PSD, B needed to be large. Consequently, this approach became computationally intensive. To reduce computation time, the step size (ss) for the Levenberg-Marquardt algorithm was set coarsely at $ss(h_0,h_1,h_2)$=(1,1,1) pixel. However, this likely reduced the accuracy of the fitted values (although we have not tested this). We discuss ways to reduce computational cost further in Section 5.

Table 3. Parameters and results of fit for Case 2 ($M < 4B$ with the PSD described by an analytical function). The initial guess and fit result are represented by nominal (range) values across the instantiations.

	h_0	h_1	h_2
Simulation	8	16	24
Initial guess	23.0 (±0.4)	23.0 (±0.4)	23.0 (±0.4)
Fit result	6.6 (±2.2)	13.1 (±3.8)	27.3 (±3.7)

4.1.3. Case 3 ($M<4B$ and $n^{el}(a,b,c)$ does not exist)

The third case, which is the most difficult, occurs when $M < 4B$ (as in Case 2) but the PSD cannot be described by a suitable analytical function. A practical example occurs when we examine a limited volume of material, resulting in poor sampling of a PSD that could be described analytically if it were better sampled. In this situation, the PSD can be sparse and discontinuous. Although it does not seem possible to achieve a complete understanding of the PSD in this situation, we describe here an approximate approach that yields some information about its characteristics.

Consider an ellipsoid with volume v^{el} oriented in a certain direction with a contour map of its corresponding XPCI power spectrum shown in Fig. 3. The contour lines represent local minima. If a line profile was drawn radially from the origin of the 2D XPCI power spectrum, it can be shown that it is equivalent to that of a sphere of population and size that depends on the angle of the line profile (ϕ) and dimensions of the ellipsoid (see Appendix A). Drawing line profiles in any other direction from the origin will similarly yield a XPCI power spectrum equivalent to some population of mono-sized spheres. Now consider the ellipsoid being one of many identical size ellipsoids randomly spatially distributed and oriented. The resultant XPCI power spectrum azimuthally averaged can now be understood to be equivalently represented by a distribution of spheres S_i given by (complete derivation is given in Appendix A):

$$S_i = \left\{ (r, n^{sp}) : r = R_i, n^{sp} = \frac{n_i^{el} v_i^{el} \sin\phi_P}{4\pi \left(v_i^{sp}\right)^2} \forall q, p \in \mathbb{N} | q = [1, Q], p = [1, P] \right\}. \quad (13)$$

Extending this to B bin size ellipsoids returns a sphere size distribution (S) of:

$$S = \left\{ \bigcup_{i=1}^{B} S_i, \bigcup_{i=1, j>i}^{B} \left(S_i \cap S_j\right) \right\}. \quad (14)$$

Set S is a concatenation of S_i to represent a distribution of spheres of size and population calculated from Eq. 14 with an XPCI power spectrum equivalent to that of B bin size ellipsoids. It can be ordered into a sphere size distribution by applying a histogram as a function of r. A typical mapping of a single ellipsoid size to its sphere size distribution is shown in Fig. 4.

Performing such a mapping for all of the bins in the ellipsoidal PSD can transform a highly non-uniform and sparse ellipsoidal PSD onto a better sampled spherical PSD, which is more likely describable by an analytical function. Consequently, Eq. 8 becomes an implicit function of the XPCI power spectrum and (r, n^{sp}), where there exists a function to describe (r, n^{sp}). Since this becomes an over-determined system of non-linear equations, the approach described for Case 1 can be used to solve for the spherical PSD.

Thus far, we have shown how a size distribution of spheres can yield the same XPCI power spectrum of any given size distribution of ellipsoids. We refer this to the “sphere model". This

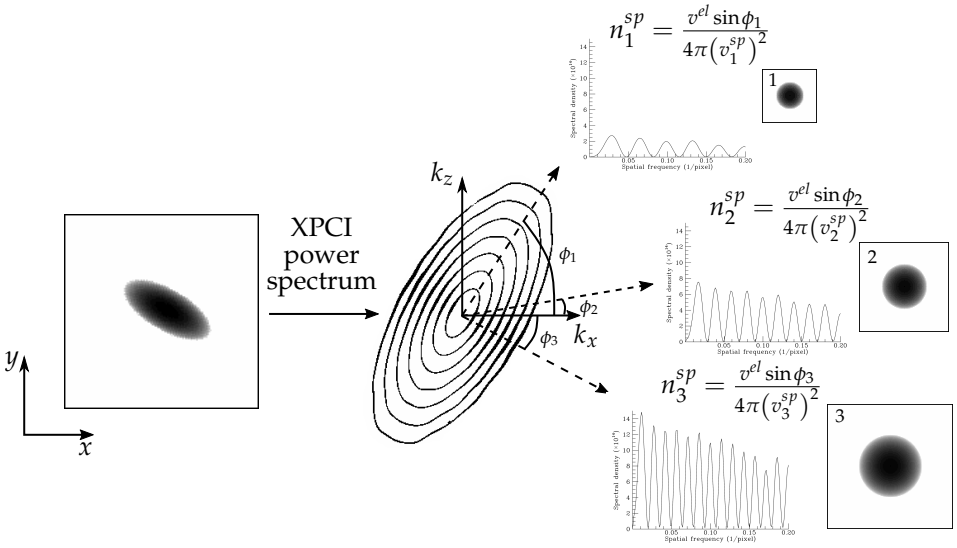

Fig. 3. Representation of an ellipsoid as a distribution of spheres via its XPCI power spectrum. A line profile from the origin of the power spectrum in any direction yields a 1D power spectrum that equivalently represents a population, n^{sp}, of mono-size spheres.

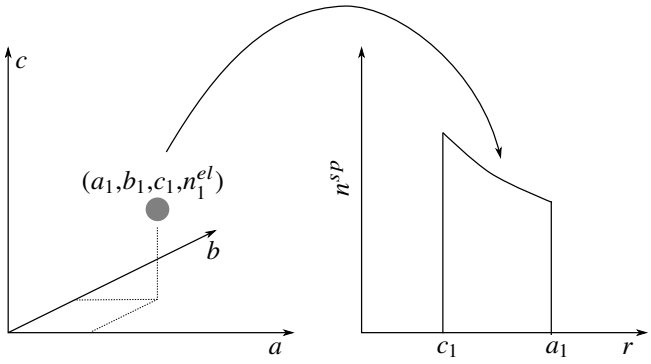

Fig. 4. The XPCI power spectrum of a single point in the ellipsoid distribution space (left), corresponding to n_1^{el} ellipsoids of a particular size (a_1, b_1, c_1), randomly oriented and spatially distributed, is equivalent to a 1D distribution of spherical pores (right), assuming that $c_i \leq b_i \leq a_i$.

is an important property since the spherical PSD is generally much easier to determine than that of an ellipsoid. While Eq. 14 shows how (r, n^{sp}) can be mapped to (a, b, c, n^{el}), a unique mapping of the spherical PSD back to the ellipsoidal PSD is not possible (unless there exists *a priori* information about the ellipsoid PSD) since the number of spherical parameters (r, n^{sp}) is less than (a, b, c, n^{el}). But we show here three properties of the ellipsoidal PSD, including the porosity (total pore volume) and trends in the number and median pore size for evolving distributions, that can be inferred from the spherical PSD.

Property 1: Sphere PSD preserves the porosity of the ellipsoidal PSD.
The total volume of ellipsoids is preserved in the total volume of spheres calculated using the sphere model; that is,

$$\frac{4}{3}\pi \sum_{(r,n^{sp})\in S} n^{sp} r^3 = \frac{4}{3}\pi \sum_{i=1}^{B} n_i^{el} a_i b_i c_i. \tag{15}$$

This is proven in Appendix B.

Property 2: Population of spheres depends on the population and aspect size ratio of ellipsoids.
The total number of spheres returned by the sphere model (N^{sp}) is greater than or equal to that of ellipsoids (N^{el}), that is:

$$N^{sp} = \sum_{(r,n^{sp})\in S} n^{sp} \geq N^{el} = \sum_{i=1}^{B} n_i^{el}. \tag{16}$$

However, information about N^{sp} can still be learned from N^{el}. To understand how, we can see from Eq. 13 that N^{sp} is a function of n^{el} and, from the remaining terms, (a, b, c). Consequently, N^{sp} is directly proportional to N^{el}. The influence of (a, b, c) on N^{sp} can be visualized by having N^{sp} normalized to a fixed value of N^{el} and plotted against a range of b/a and c/a (and not for a range of a, b, and c since it does not depend on them independently.) in Fig. 5. For $a = b = c$, $N^{sp}/N^{el} = 1$ as expected because the ellipsoids in the model are actually spheres. Elsewhere, $N^{sp}/N^{el} > 1$ and the sphere model overestimates the true number of pores in the material. This dependence of N^{sp}/N^{el} on the aspect ratio of the ellipsoids means that any change in N^{sp} measured using the sphere model could reflect an actual change in N^{el}, their aspect ratio, or both.

Property 3: Median sphere radius is a monotonic function of the median ellipsoid radius.
Turning now to the size of the pores, we note that both the median ellipsoid radius m_{el}:

$$\frac{\sum_{r=0}^{m_{el}} \text{hist}\{E\}(r)}{\sum_{r=0}^{\infty} \text{hist}\{E\}(r)} = 0.5, \tag{17}$$

where

$$E = \left\{ \bigcup_{i=1}^{B} E_i, \bigcup_{i=1, j>i}^{B} \left(E_i \cap E_j\right) \right\} \tag{18}$$

and

$$E_i = \left\{ (R_i, n_i^{el}) : \theta = \left\{\frac{q\pi}{Q}\right\}, \phi = \left\{\frac{p2\pi}{P}\right\} \forall q, p \in \mathbb{N} | q = [1, Q], p = [1, P] \right\}, \tag{19}$$

and the median sphere radius m_{sp} returned by the sphere model,

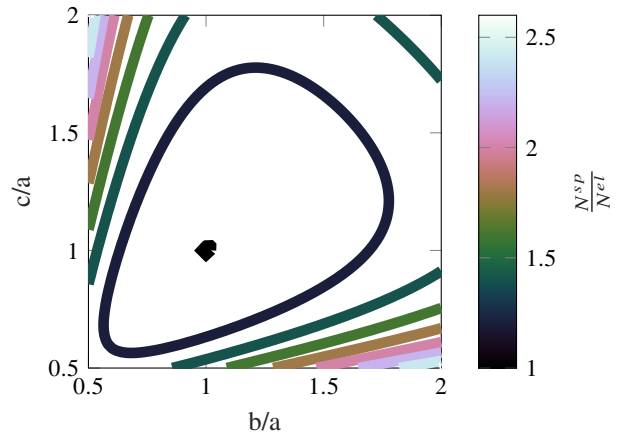

Fig. 5. The total number of spheres N^{sp} in the sphere model normalized to a fixed total number of ellipsoids N^{el} in the material, for different aspect ratios of ellipsoids b/a and c/a.

$$\frac{\sum_{r=0}^{m_{sp}} \text{hist}\,\{S\}\,(r)}{\sum_{r=0}^{\infty} \text{hist}\,\{S\}\,(r)} = 0.5, \tag{20}$$

depend on the aspect ratio of the ellipsoids b/a and c/a (and, of course, on a). Figure 6 shows plots of both as functions of aspect ratio (for $a = 1$). While m_{el} and m_{sp} never equate to each other, both increase monotonically with b/a and c/a, as well as with a (not shown). Consequently, variation in the median sphere radius measured by the sphere model generally follows the same direction as that of the pores, except when the directional derivative of either is zero. Normally, samples such as sandstone contain a distribution of pores that are unlikely to all follow along the direction that results in zero change in their median radius, from either the ellipsoidal or spherical PSD. Therefore, the median pore and sphere radius track together, except in unusual cases.

To demonstrate case 3, consider a model consisting of 200 different ith bin ellipsoids in a $2.2 \times 2.2 \times 2.2$ mm^3 volume of material. The parameters $(a_i, b_i, c_i, n_i^{el})$ of each ith size ellipsoid are randomly generated from four uniformly-distributed random numbers $n^{el} \in \mathbb{N} \cap [10, 60]$ and $a, b, c \in \mathbb{R} \cap [32.5\ \mu\text{m}, 162.5\ \mu\text{m}]$. The ellipsoidal PSD (Fig. 7(a)) for this model is sparse and cannot be represented as an analytical function, and because $M < 4B$ the XPCI image does not provide sufficient information to solve for the ellipsoidal PSD uniquely. However, using the sphere model in Eq. 13 we convert the 3D ellipsoidal PSD into a spherical PSD, as shown by the solid blue line in Fig. 7(b). This 1D distribution can be described by an analytical function; here we use the Pearson VII distribution function introduced as Eq. 11 but with the independent variable k replaced with r.

To determine if we can solve for the spherical PSD from the XPCI power spectrum using Eq. 8, we simulate the XPCI image for the model material; the resulting XPCI power spectrum is shown as the solid blue line in Fig. 7(c). We then use the least-squares method to fit the calculated XPCI power spectrum from the sphere model (assuming the Pearson VII distribution) to that simulated. The result is shown as the dashed red line in Fig. 7(c). The good agreement shows promise that the correct spherical PSD can be determined from a single XPCI image, though further testing is required for different porous materials.

Using the best-fit values of the parameters from the Pearson VII distribution we then calculate the fitted spherical PSD. The result is shown as the dashed red line in Fig. 7(b). The agreement is reasonable for pore sizes above about 20μm; below that size, the lack of a maximum in the

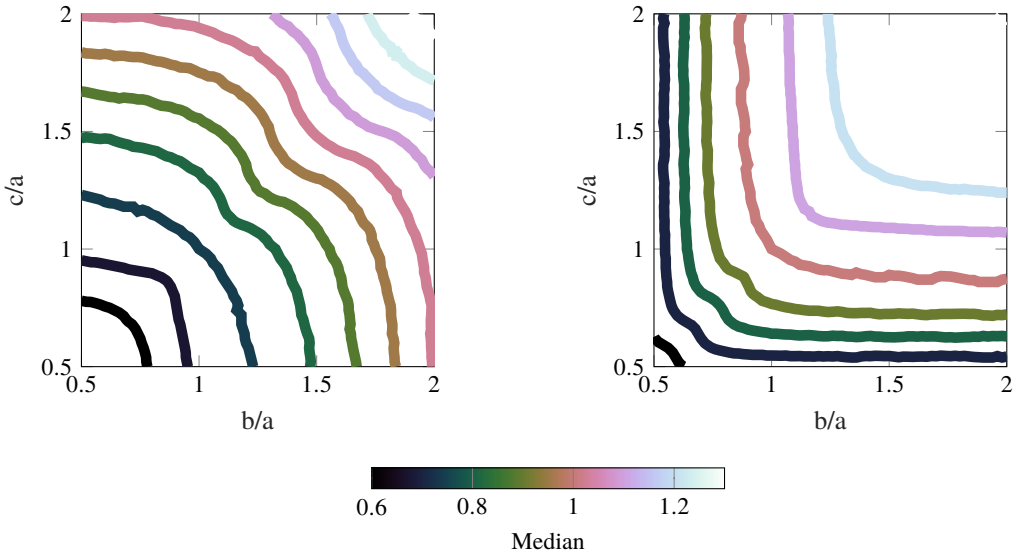

Fig. 6. The median ellipsoid radius m_{el} (left) and median sphere radius m_{sp} (right) as functions of ellipsoid aspect ratios $(b/a, c/a)$ with $a = 1$.

Pearson VII distribution for $r > 0$ causes it to diverge from the simulated spherical PSD.

Table 4 compares several structure parameters calculated directly from the ellipsoidal PSD with the sphere PSDs, one converted directly from the ellipsoidal PSD (solid blue line in Fig. 7(b)) and the other from fitting to the XPCI power spectrum (dashed red line in Fig. 7(b)). As expected based on the three properties of the sphere model, total porosity is preserved; that is, the total porosity calculated from both sphere PSDs match that calculated directly from the actual ellipsoidal PSD. Also as expected, the number and radius of pores from the spherical PSDs do not match those of the underlying ellipsoidal PSD (although the values between the spherical PSDs do match). Neither quantity can be determined from the sphere model, unless the aspect ratio of the ellipsoids is known *a priori*.

Table 4. Case 3: Comparison of ellipsoid and sphere PSDs.

	Ellipsoid	Sphere (calculated)	Sphere (fitted)
Porosity (%)	29.33 (±0.01)	29.04 (±0.01)	31.60 (±0.02)
Number	7037 (±211)	11162 (±477)	10694 (±671)
Median radius (μm)	15.5 (±0.2)	10.2 (±0.3)	10.7 (±0.8)

Although we cannot extract true values of the number of pores or their median radius from the sphere model, we can say something about how they evolve over time in a dynamic system. To show this, we simulate a sequence of XPCI images of a model material. We begin with the same ellipsoidal PSD as that used to demonstrate case 3 but in a larger volume of $3.58 \times 3.58 \times 3.58$ mm^3 volume of material. The subsequent states of the sample are generated by incrementally changing the aspect ratio and number of pores. This sequence mimics volumetric dilation of a sandstone, increasing the pore radius and opening up new pores. At each step we calculate the true porosity, number of pores, and median pore radius directly from the actual ellipsoidal PSD. At each step we

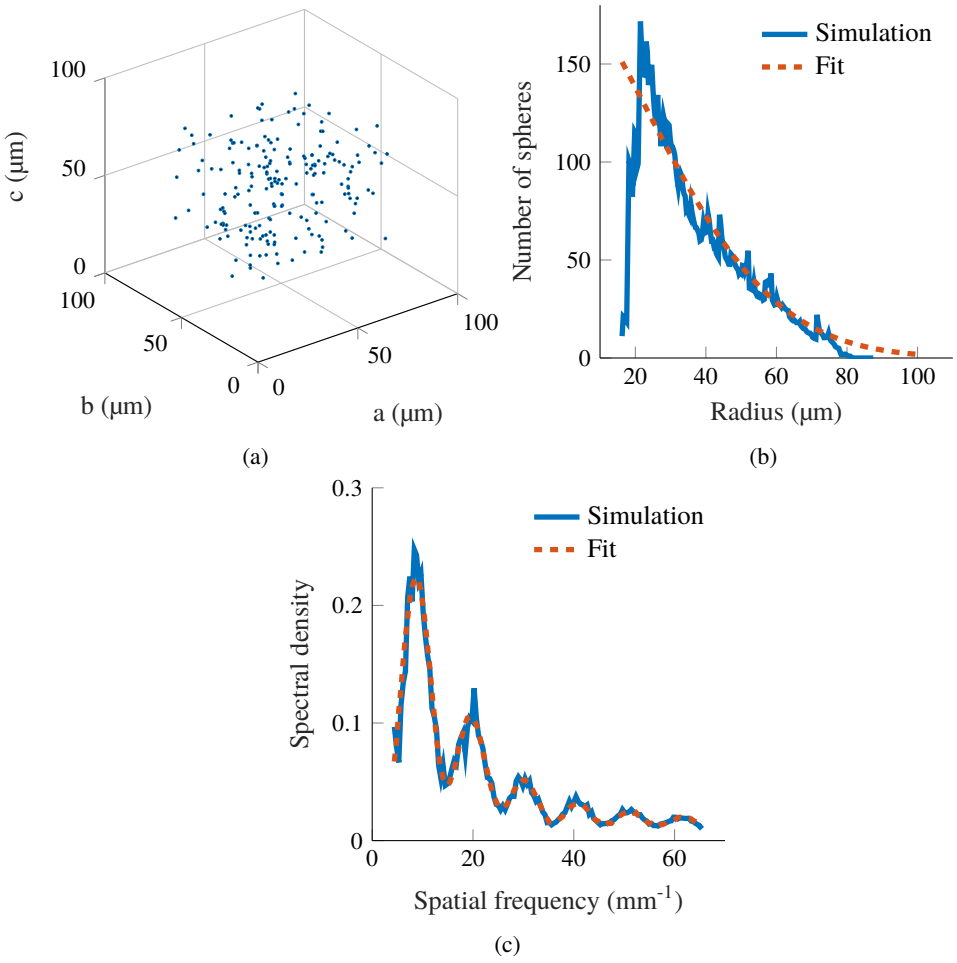

Fig. 7. Case 3, a sparse PSD. (a) 3D Ellipsoid PSD for the model material. Comparison of the (b) spherical PSD and (c) XPCI power spectrum between that simulated from a model porous material (solid blue line) and that fitted to the simulated XPCI power spectrum using the sphere model (dashed red line).

also calculate the same parameters from the spherical PSD directly converted from the ellipsoidal PSD using Eq. 13 of the sphere model. The parameters calculated on the basis of the sphere model are thus exact (in the sense that they are uniquely determined by the ellipsoidal PSD) but, because of the three properties described above, they differ from the true values determined directly from the ellipsoidal PSD. Finally, at each step we also simulate the XPCI image from the model, and use this as the basis for obtaining a best-fit spherical PSD (using the Pearson VII distribution function for the spherical PSD, as above).

The results of this exercise are shown in Fig. 8, where the solid blue line is the value of each parameter calculated directly from the ellipsoidal PSD used to create the model, the dashed red line is the value calculated from the model on the basis of the spherical PSD, and the dash-dotted yellow line is the result obtained from the fits to the simulated XPCI power spectra. We see that the agreement for the total porosity (part (a) of the figure) is good, as expected because total porosity is conserved in the sphere model as discussed above. There is a slight increasing discrepancy in the porosity because of the gradual breakdown of the weakly absorbing and scattering assumption. As expected, neither the number of pores (b) nor the median pore radius (c) from the sphere model agrees with the true values, but (significantly) *trends* in both are captured.

It is also possible to extract information about the behavior of the ellipsoid aspect ratios from the sphere model. For instance, let us assume one or more of the semi-axes, and the number of ellispoids, is unchanged, such as during uniaxial compression/tension tests of porous materials. Then, after calculating the total number and median sphere size over time, we compare their trends to Figs. 5 and 6. If both number and median sphere size are increasing then it means the aspect ratio is increasing, and vice versa. Another interesting observation is if the number of spheres is increasing but the median sphere radius remains unchanged, then only one of the aspect ratios is changing.

4.2. Experimental validation on sandstone

In this section we describe experimental validation of the third case above, using the sphere model to investigate a sparse PSD in Berea sandstone. To do so, we collected complete computed tomography (CT) data sets from which we extracted the 3D pore distribution and converted into spherical PSD using Eq. 13 of the sphere model, and compared that with the spherical PSD calculated from fitting to the XPCI power spectrum of single 2D XPCI images.

The samples for this study are 3.1 mm^3 cuboids of Berea sandstone (Kocurek Industries, Inc.). Berea sandstone is >90% quartz, with small amounts of feldspar and metal oxides [35]. For the purposes of the calculations we take it to be 100% quartz. The porosity reported by the distributor is 18-21%. Using the single image phase retrieval algorithm [30], we calculated the maximum variation in thickness perpendicular to the x-ray direction of the Berea sandstone samples to be ~0.22 mm to show that the weakly absorbing condition, $\mu\Delta G_z(\vec{r}_\perp) \approx 0.14$, and the weakly scattering condition, $\frac{a_L}{L\lambda|\nabla_\perp\phi|_{\max}} \approx 2.8$, where $a_L \approx 23$ μm as measured using CT described below, are satisfied.

We performed CT XPCI imaging at beam line 2-BM of the Advanced Photon Source with an x-ray beam tuned by a W/BC4 multilayer monochromator to 20.4 keV. The sample-to-detector propagation distance was 0.1 m and the image pixel size set to 3.25 μm. A total of 1500 XPCI images are recorded over 180° for each sample to reconstruct their 3D 'attenuation map' using filtered back projection with a Shepp-Logan filter [36]. XPCI images do not reconstruct a true attenuation map but the overall 3D structure is preserved. XPCI is chosen for performing CT because it enhances the boundary of the reconstructed pores, thus increasing the accuracy in isolating the pores [37].

To isolate the pores and measure their sizes, we performed the following data manipulation on the 3D data sets: (1) image binarizing with a threshold value calculated using Otsu's method to

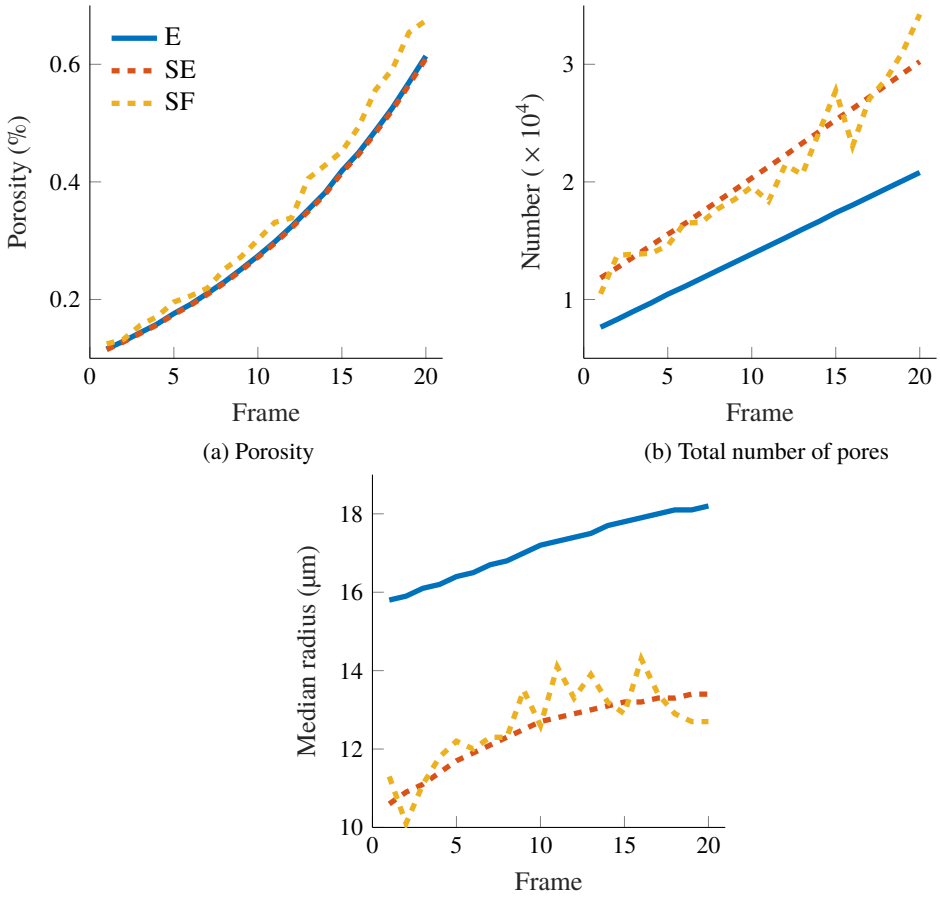

(a) Porosity

(b) Total number of pores

(c) Median pore radius

Fig. 8. Effectiveness of the sphere model in capturing, from single simulated XPCI images, trends in (a) porosity, (b) total number of pores, and (c) median pore size. In each figure, the solid blue line is an exact calculation based on the true ellipsoid size distribution (E), the dashed red line is a calculation from the equivalent sphere size distribution from the model (SE), and the dash-dotted yellow line is the value obtained from a best-fit of the simulated XPCI power spectrum (SF), assuming a Pearson VII distribution of spherical pores.

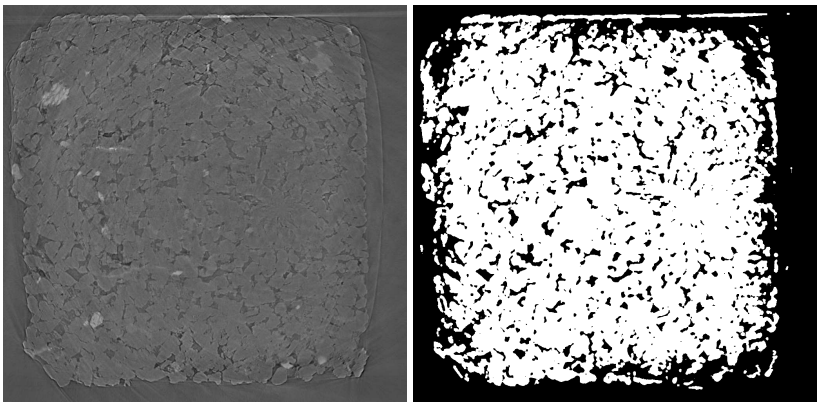

(a) (b)

Fig. 9. CT slice of Berea sandstone (a) before and (b) after image thresholding and filtering.

separate the pores and material (quartz and inclusions); (2) re-categorizing pores with fewer than three 8-point connected voxels as material, since it is found that many of them are misidentified during binarization due to image noise and artefacts; (3) performing morphological opening with a two-voxel size cuboid to remove pores and parts of pores with size dimensions of one pixel; and (4) performing morphological closing with a three-voxel-radius spherical structural element to join disconnected voxel clusters into single pores. A single CT slice is shown in Fig. 9 before and after these thresholding and filtering operations.

We use the image processed CT data as a material model $G(\vec{r})$ to simulate its XPCI power spectrum to compare with that experimentally recorded (which is from one of the CT XPCI projections) as a way to validate that the pores are correctly isolated. To simulate the XPCI image of the CT data, we projected the CT data to calculate $G_z(\vec{r}_\perp)$ and simulated the corresponding XPCI image using the angular spectrum method described in section 4.1. We measured the attenuation coefficient (μ) of quartz from the CT image by image thresholding to isolate voxels not enclosing pores and away from phase contrast-affected boundaries, then averaged over those voxels to give $\mu = 611$ m^{-1}. In comparison, pure quartz is $\mu = 451$ m^{-1} at 20.4 keV, which likely indicates other materials are mixed with quartz in Berea sandstone. We used this in the single material phase retrieval algorithm [30] for calculation of the attenuation image $I(\vec{r}_\perp, z = 0)$, normalize it against the XPCI image, to simulate the XPCI power spectrum.

The resulting XPCI power spectrum, calculated from the CT data after the binarization and filtering operations described above is shown in Fig. 10(a), together with the measured power spectrum from a single experimentally recorded XPCI image. The agreement is not good, mostly because many of the pores are highly irregularly shaped. This results in their surfaces being poorly discretized. Consequently, they are not accurately simulated in the XPCI power spectrum. To address this, we watershedded the image to fit an ellipsoid to each pore, and used second-order moments, rescaled to match the pore volume, to calculate the three semi-axis lengths (a, b, c) of each fitted ellipsoid. This procedure resulted in significantly better agreement between the XPCI power spectrum calculated from the CT data and that from the XPCI image (Fig. 10(b)). This shows that even though the pores are not exactly ellipsoidal, it captures their overall shape and size, resulting in accurate simulation of their XPCI power spectra. The fitted ellipsoids are converted into equivalent spheres using the sphere model to show that their XPCI power spectrum also agrees well with that computed from experimentally recorded XPCI images.

The ellipsoidal PSD measured from the filtered and watershedded CT image is shown in

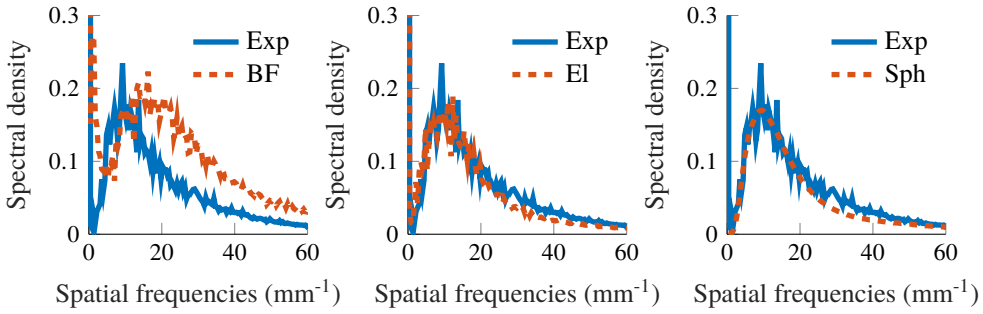

Fig. 10. Comparison of experimentally recorded XPCI power spectrum (Exp) with that simulated from a CT image of Berea sandstone after (a) binarization and filtering to isolate the pores (BF), then (b) replacing the pores with fitted ellipsoids (El), and then (c) replacing fitted ellipsoids with spheres using the sphere model (Sph).

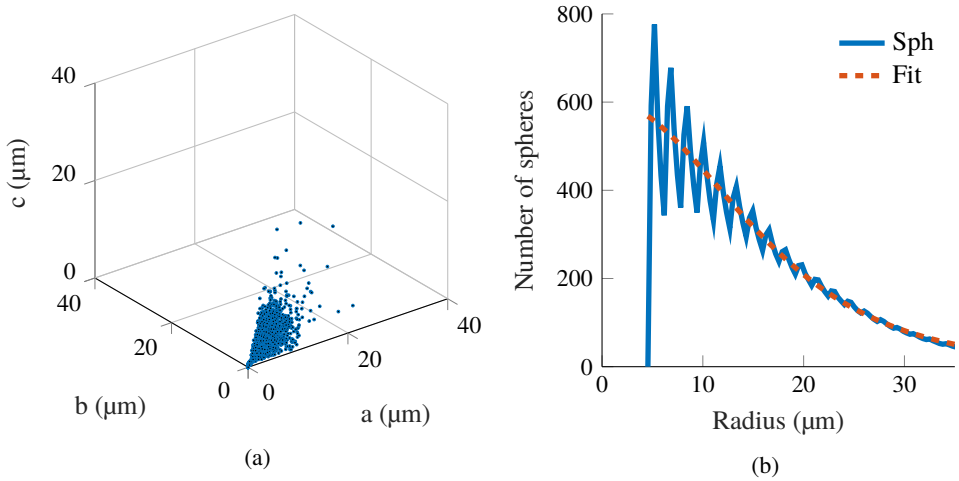

Fig. 11. (a) Ellipsoid PSD for Berea sandstone, derived from 3D CT data as described in the text. (b) The corresponding spherical PSD directly converted from the ellipsoidal PSD, the size dimensions of which has been rescaled to match the pore volume, and from fitting to the XPCI power spectrum.

Fig. 11(a). The large number of discrete pore sizes (B) means that the number of unknowns in the model ($4B$) exceeds the number of spatial frequencies sampled (M), so Case 1 described above does not apply. Moreover, the ellipsoid sizes are sparsely distributed, particularly at larger sizes, making it difficult to describe the ellipsoidal PSD with a 3D function (Case 2). Therefore, we turn to Case 3, the sphere model. As in the examples described above, we approximate the spherical PSD by the Pearson VII distribution function, the parameters of which are found using Eq. 11. The spherical PSD is calculated from solving for those parameters by fitting its simulated XPCI power spectrum to that experimentally recorded. Figure 11(b) shows that this fitted spherical PSD (red dashed line) compares well with that directly calculated from the CT images (solid blue line).

Table 5 shows structural properties of Berea sandstone (porosity, total pore number, and median pore radius) derived from the CT data and from the power spectrum of a single XPCI image using

the sphere model (Case 3). The first column shows values determined from the watershedded CT data, in which the irregularly-shaped pores are replaced by ellipsoids of equivalent volume. From the PSD of the ellipsoids we can calculate the equivalent PSD for spheres using Eq. 13, the results of which are given in the second column. Notice that this calculation preserves the total porosity but not the number or median radius of the pores, as expected from the three properties of the sphere model described above. Finally, the third column shows the result of a least-squares fit of the spherical PSD model to a single 2D XPCI image; the agreement with the spherical PSD calculated directly from the 3D data is good.

The uncertainty in the 3 parameters calculated from the ellipsoidal PSD is from the uncertainty in segmenting the pores; in particular, in categorizing pores containing $\leq$3 8-point connected voxels as material. This value of three was arbitrarily chosen, hence the uncertainties correspond to using 3 ± 2 8-point connected voxels. The expected spherical PSD is directly converted from the ellipsoidal PSD and hence the uncertainty in the three parameters are also from segmenting the pores. For the fitted spherical PSD, the main source of uncertainty is image noise. This is already measured for determining the pixel size used to simulate our XPCI sandstone images. Note that the median sphere size uncertainty of the calculated and fitted sphere PSD are insignificant.

In comparing the porosity measured by the three PSDs, they are similar as expected, but not within the range of their uncertainties. The larger porosity measured by the ellipsoid and calculated spherical PSD is likely due to the application of a morphological closing operator on the CT image. This is a necessary step to correct for oversegmentation of pores but unfortunately slightly enlarges them. None of the porosities measured by the PSDs is close to that provided by the manufacturer: 18-21%. This was measured using a water saturation approach, which is a highly accurate technique. The discrepancy is then due to the limited spatial resolution of the CT images, which is ~6.5 μm (2 pixels). Shi *et al.* [38] showed using much higher resolution CT that approximately 40% of the total pore volume in Berea sandstone is occupied by pore sizes less than 6.5 μm. This would account for the discrepancy in porosity and consequently means the spatial resolution of our technique is limited by that of the 2D XPCI image. The number of pores measured between the calculated and fitted sphere are within uncertainty, while that of the median pore radius is not due to the morphological closing operator. Thus, having proven our technique can reasonably calculate the spherical PSD of real porous materials, it can be applied in future dynamic studies to calculate pore porosity and trends in the number and median size pore.

Table 5. Structural properties of Berea sandstone. ***Watershedded CT*** **refers to values calculated from the watershedded x-ray CT data, in which the irregularly-shaped pores are represented by ellipsoids of equivalent volume.** ***Sphere (calculated)*** **refers to values of a sphere size distribution that is converted from the CT data-computed ellipsoidal size distribution.** ***Sphere (fitted)*** **refers to values obtained from a spherical PSD calculated from fitting its simulated XPCI power spectrum to that experimentally measured.**

	Watershedded CT	Sphere (calculated)	Sphere (fitted)
Porosity (%)	12.7±0.6	12.7±0.6	11.3±0.4
Number	$(1.7 \pm 0.3) \times 10^4$	$(4.20 \pm 0.7) \times 10^4$	$(3.94 \pm 0.01) \times 10^4$
Median radius (μm)	23.4±1.6	10.4	10

5. Discussion

A knowledge of the true pore (or particle) size distribution of a material requires 3D microstructural data derived, for example, from x-ray computed tomography. The basic result of this work is an approximate description of the PSD for the case where only a single 2D XPCI image is available, such as might be obtained during a dynamic study of an evolving material. One example of this situation would be a granular material subjected to dynamic mechanical loading.

Equation 8 describes an implicit relation between the XPCI power spectrum and the pore PSD. In deriving this expression, we assumed that the pores are ellipsoidal, with random positions and orientations, embedded in a material of uniform x-ray refractive index. (We note that this approach is equally applicable to the inverse situation — ellipsoidal particles in air.) We described three approaches, for different assumptions about the nature of the PSD, to solving the implicit function and calculating the PSD from a single 2D XPCI power spectrum. For the last, and most challenging situation, we also demonstrated with experimental data from Berea sandstone. The advantages and limitations of each of these approaches will be discussed.

The first approach solves the independent variables $(a_i, b_i, c_i, n_i^{el})$ for each of B bins in the ellipsoidal PSD. This has potential applications in measuring PSD of a finite number of highly controlled pore sizes, such as in additive manufactured materials and targeted drug delivery carriers [39, 40]. One disadvantage of this approach is that the number of different size ellipsoids (bins) must be known beforehand. Furthermore, for a unique solution to exist the number of bins must be small enough that the total number of independent variables ($4B$) is less than that of spatial frequencies (M) sampled in the XPCI power spectrum. This is true only in limited situations. We showed in Table 2 that the result of our fitted parameters are not in complete agreement due to image noise and breakdown of the weakly-absorbing material condition. The former can be solved using a noise model that accounts for the correlation with the material (for example, see [41]), while the latter can be rectified by imaging at a higher x-ray energy.

The second approach overcomes this limitation by assuming the PSD can be described by a continuous 3D distribution function. Beginning with an initial guess of the parameters of the 3D distribution function, Eq. 8 is iteratively solved to calculate the best fit parameters. The types of 3D distribution functions that Eq. 8 can uniquely solve are limited to those with spherical averages having a one-to-one mapping with the parameters. For example, multiple 3D Gaussian functions can spherically average to the same 1D Gaussian function. Consequently, multiple solutions for the PSD exists. To ensure a unique solution, either appropriate choice of a 3D distribution function and/or constraint on the parameters is needed. Another limitation is case 2 is computationally intensive. Our solution was to increase the step size at the expense of accuracy and limit the range of spatial frequency to which to fit. As future work, a library of XPCI power spectra could be pre-calculated. Although the number of such power spectra required can become exceedingly high, for example, a PSD with ellipsoid axes lengths ranging from 0 to 200 μm sampled at 0.1 μm requires 8×10^9 pre-calculations of different size ellipsoid bin XPCI power spectra, these only need to be computed once.

The third approach is computationally more efficient than the second approach because it is based on simulation of the XPCI power spectra for spheres rather than ellipsoids during least-squares fitting. To explain further, an ellipsoidal PSD with a, b, c each sampled d times requires d^3 XPCI power spectra calculations but for the corresponding spherical PSD only d XPCI power spectra are required. The major limitation to this approach is that the spherical PSD is not a direct representation of the ellipsoidal PSD. However, we showed that it does accurately capture the porosity and the trend in the median pore radius. We also showed the model captures the trend in the total number of pores, so long as their aspect ratios do not change appreciably. There are many applications such as the measure of alveolar PSD [23], where the aspect ratios do not change appreciably and hence the trend in the number of spheres approximately follows that of the pores. The mean pore radius is also another parameter of interest; however, neither its

value or trend are preserved between the ellipsoidal and spherical PSD.

Our algorithm was tested by calculating the pore PSD of Berea sandstone measured from experimental XPCI images. Since the PSD contains a large range of sparsely distributed pore sizes, the third approach was chosen. With the CT images providing a direct measure of the PSD, we validated our algorithm in accurately measuring the spherical PSD using the sphere model from a single 2D XPCI image. Our algorithm was tested on multiple Berea sandstone samples to evaluate its robustness (not shown). It was found that the PSD did not always match in overall shape with that directly measured using CT. It is possible that either the CT is not a robust measure of the PSD because of the pore sizes being at the CT spatial resolution limit and/or our algorithm may be sensitive to image noise, which causes fluctuations in the XPCI power spectrum.

When our algorithm does accurately measure the PSD, it is important to emphasize that it is accurate within the spatial resolution of the XPCI image. Although spatial resolution can be increased in the experiment, this is often at the expense of a smaller field of view, thus limiting measurements of the larger pores. Analyzer-based XPCI could be a viable solution [42]. It can record and separate intensity signals from pores above and below the image resolution limit. The pore PSD measured separately from each signal can be collated to give the complete pore PSD.

In demonstrating the three approaches it is found that the second and third approach are inundated with local minima. This suggests that a unique solution may not always exist even if the number of unknowns is less than that of independent equations. It was raised earlier that the M equations may not be independent. Further investigation is required to derive how PSDs map to their XPCI power spectra. If the mapping is not one-to-one it is possible that bounding the domain of PSDs by an analytical function or adding a regularizer can lead to a unique solution. Our choice of using Eq. 12 for the second approach and Eq. 11 for the third approach may not have sufficiently bounded the PSD to avoid encountering multiple local minima.

Other assumptions of the model may also not hold in particular situations. For example, we assumed that the ellipsoidal pores are randomly spatially distributed and oriented, which may not be the case in many materials. Even when it is, there is a further assumption that enough pores are sampled to achieve a suitably uniform sampling of orientations and positions. This may not be true if the sample volume is small (and hence only a small number of pores are sampled). We can, however, check the assumption of random orientation by looking for anisotropy in the measured 2D XPCI power spectrum. We note that a possible future extension of the model would be to use the anisotropy of the XPCI power spectrum to derive information about anisotropic pore orientations. When pores become densely packed, the assumption that the pores are randomly distributed breaks down and short-range order comes into effect. This could be accounted for and measured, as has already been done by Leong and coworkers [23].

Turning to experimental considerations, we note that our algorithm does not account for the effect of motion blur. Furthermore, in dynamic imaging it is often necessary to use partially coherent, polychromatic x-ray beam and image outside the near-field regime to provide sufficient image contrast to overcome noise problems. Equation 8 breaks down at these experimental conditions, but it could be extended to laboratory-based x-ray sources if the energy spectrum and detector response is known [43]. There are also transport-of-intensity equations, on which Eq. 8 is based, that have been extended beyond the near-field regime so that XPCI images can be recorded outside the near-field regime for better image contrast [24].

6. Conclusions

We derived an implicit analytical expression relating a 3D PSD to the XPCI power spectrum of a single XPCI image of a given material, assuming randomly oriented and spatially distributed ellipsoidal pores imaged with a spatially coherent monochromatic x-ray beam in the near-field regime. We described three approaches to using this expression to solve for the PSD from a single

2D XPCI image. The first is applied when the number of unknown PSD variables (semi-axis lengths and population) is less than the number of spatial frequencies sampled in the XPCI power spectrum. When the converse occurs, the PSD can be found if it can be described by an analytical function. If not, then the pores can be modeled as spheres. While the spherical PSD is not equivalent to the ellipsoidal PSD, it can still provide information about the total porosity as well as trends in the number and median radius of the pores. We successfully demonstrated each approach to solving for the pore PSD with simulated XPCI power spectra of porous materials. We further tested our algorithm using experimental data from Berea sandstone. Although the pores in this material are not truly ellipsoidal, our algorithm can still reliably capture information about the PSD. Moreover, the model makes several simplifying assumptions and has important limitations, but we expect that it will be broadly useful in contexts where 3D microstructural data is unavailable, and inferences about the 3D structure must be made based on projected 2D data. An important example of such a situation is for rapidly-evolving systems, where there is insufficent time to obtain sufficient data for 3D reconstructions.

Appendix A: Derivation of the sphere model

We derived Eq. 8 relating an ellipsoidal PSD to its XPCI power spectrum. One useful application of this equation is solving for the ellipsoidal PSD from a given XPCI power spectrum. However, a unique solution is not guaranteed. An example of this was presented as case 3 where a unique solution does not exist if the number of independent equations (i.e., the number of spatial frequencies sampled in the XPCI power spectrum) is less than that of unknowns in the ellipsoidal PSD, in addition to lacking an analytical function to adequately describe the ellipsoidal PSD. In response, we qualitatively justified that the XPCI power spectrum can provide a unique solution if a spherical PSD is assumed instead. While the spherical PSD cannot be trivially mapped back to the ellipsoidal PSD, some information about the ellipsoidal PSD can be extracted. We presented an expression for the spherical PSD (Eq. 13) without proof in terms of the ellipsoidal PSD and showed how their porosity, total number and median size of the ellipsoids/spheres are related. In this appendix, we provide the proof for Eq. 13.

To begin, we re-write Eq. 8 for the XPCI power spectrum of B bin ellipsoids (a_i,b_i,c_i,n_i^{el}) spatially distributed and oriented randomly:

$$\left|\mathcal{F}\left\{\frac{I(\vec{r}_\perp, z=L)}{I(\vec{r}_\perp, z=0)}-1\right\}\right|^2 = \frac{L^2\delta^2k^4}{4\pi}\sum_{i=1}^{B}\left[\sum_{p=1}^{P}\sum_{q=1}^{Q}\frac{n_i^{el}v_i^{el}\sin\phi_p}{\left(v_i^{sp}\right)^2} \times\left|\frac{v_i^{sp}}{(R_ik)^2}\left[\frac{\sin(R_ik)}{R_ik}-\cos(R_ik)\right]\right|^2\right], \tag{21}$$

where

$$v_i^{sp} = \frac{4}{3}\pi R_i. \tag{22}$$

We introduce the XPCI power spectrum of W different size spherical pores/particles randomly distributed spatially [21]:

$$\left|\mathcal{F}\left\{\frac{I(\vec{r}_\perp, z=L)}{I(\vec{r}_\perp, z=0)}-1\right\}\right|^2 = L^2\delta^2k^4\sum_{j=1}^{W}n_j^{sp}\left|\frac{v_j^{sp}}{(r_jk)^2}\left[\frac{\sin(r_jk)}{r_jk}-\cos(r_jk)\right]\right|^2, \tag{23}$$

where n_j^{sp} is the number of spheres of radius r_j in the jth bin of the spherical PSD.

Inside the large square brackets of Eq. 21, the expression can be transformed into Eq. 23 by making the following change of variable:

$$n_{i,p,q} = \frac{n_i^{el} v_i^{el} \sin\phi_p}{4\pi \left(v_i^{sp}\right)^2}. \tag{24}$$

We can then reduce p and q to a single index j by applying some arbitrary pairing function (its explicit form is unimportant for this proof) [44] so that:

$$n_{i,p,q} \mapsto n_{i,j}^{sp} \tag{25}$$

and

$$R_i(\theta_p, \phi_q) \mapsto r_{i,j}. \tag{26}$$

Equation 21 can now be rewritten as:

$$\left|\mathcal{F}\left\{\frac{I(x,y,z=L)}{I(x,y,z=0)} - 1\right\}\right|^2 = L^2\delta^2k^4 \sum_{i=1}^{B}\sum_{j=1}^{W} n_{i,j}^{sp} \left|\frac{v_{i,j}^{sp}}{(r_{i,j}k)^2}\left[\frac{\sin(r_{i,j}k)}{r_{i,j}k} - \cos(r_{i,j}k)\right]\right|^2, \tag{27}$$

where $W = Q \times P$.

Equation 27 shows each ith bin ellipsoid pore can be expressed as a distribution of W spherical pores. Therefore, we finally arrive at the desired spherical PSD for a single ith bin ellipsoid:

$$S_i = \left\{(r, n^{sp}) : r = R_i, n^{sp} = \frac{n_i^{el} v_i^{el} \sin\phi_p}{4\pi \left(v_i^{sp}\right)^2} \forall q, p \in \mathbb{N} | q = [1, Q], p = [1, P]\right\}, \tag{28}$$

and for B bin size ellipsoids:

$$S = \left\{\bigcup_{i=1}^{B} S_i, \bigcup_{i=1, j>i}^{B} \left(S_i \cap S_j\right)\right\}. \tag{29}$$

Appendix B: Proof that the sphere model preserves pore/particle porosity

Here we prove property 1 of the sphere model, which is,

$$\frac{4}{3}\pi \sum_{(r,n^{sp})\in S} n^{sp} r^3 = \frac{4}{3}\pi \sum_{i=1}^{B} n_i^{el} a_i b_i c_i, \tag{30}$$

where all symbols are defined in the main text.

We first prove that the total volume of a random spatial distribution and orientation of ellipsoids is equal to the corresponding total volume of spheres returned by Eq. 13 of the sphere model. Equation 30 would then automatically hold true for a size distribution of ellipsoids.

From Eq. 13, the total volume of spheres is computed by summing over the set S_i. This is more easily done by treating the variables as continuous,

$$\lim_{Q,P\to\infty} \frac{4}{3}\pi \sum_{(r,n^{sp})\in S_i} n^{sp} r^3 = \frac{4}{3}\pi \int_0^{2\pi}\int_0^{\pi} \frac{n_i^{el} v_i^{el} \sin\phi}{4\pi \left(v_i^{sp}(\theta_q, \phi_p)\right)^2} R_i^3(\theta, \phi) d\phi d\theta. \tag{31}$$

We then perform an integration by substitution by making the change of variable, $u = \cos\phi$, and integrate over $u = [-1, 1)$ to arrive at

$$= \frac{2(a_i b_i)^2 c_i n_i^{el}}{3} \int_0^{2\pi} \frac{1}{(a_i^2 - b_i^2)\cos^2\theta + b_i^2} d\theta.$$

Finally, integrating over $\theta = (0, 2\pi]$ gives

$$= \frac{2(a_i b_i)^2 c_i n_i^{el}}{3} \left[\frac{\tan^{-1}\left(\sqrt{\frac{b_i^2}{a_i^2}} \tan\theta\right)}{a_i b_i} \right]_0^{2\pi} \tag{32}$$

$$= \frac{4\pi}{3} n_i^{el} a_i b_i c_i. \tag{33}$$

This concludes the proof that the total volume of a random spatially distributed and oriented ellipsoids from a single bin size is preserved in the sphere model. This is true for any ellipsoid bin size and therefore by extension Eq. 30 holds true for B bin size ellipsoids.

Funding

Defense Threat Reduction Agency (HDTRA1-15-1-0056); Army Research Laboratory (W911BF-12-2-0022); U.S. Department of Energy Office of Science (DE-AC02-06CH11357).

Acknowledgments

We gratefully acknowledge Y.H. Sun for assistance with data collection at the Advanced Photon Source. The content, views, and conclusions contained in this document are those of the authors and should not be interpreted as representing the official positions or policies, either expressed or implied, of the Defense Threat Reduction Agency, the Army Research Laboratory, or the U.S. Government. The U.S. Government is authorized to reproduce and distribute reprints for government purposes notwithstanding any copyright notation herein. This publication is based upon data collected at the beam line 2-BM at the Advanced Photon Source, Argonne National Laboratory. This research used resources of the Advanced Photon Source, a U.S. Department of Energy (DOE) Office of Science User Facility operated for the DOE Office of Science by Argonne National Laboratory under Contract Bo. DE-AC02-06CH11357.

References

1. W. B. Lindquist, A. Venkatarangan, J. Dunsmuir, and T. F. Wong, "Pore and throat size distributions measured from synchrotron X-ray tomographic images of Fontainebleau sandstones," J. Geophys. Res-Sol Ea **105**, 21509–21527 (2000).
2. O. Mohnke and B. Hughes, "Jointly deriving NMR surface relaxivity and pore size distributions by NMR relaxation experiments on partially desaturated rocks," Water Resour. Res. **50**, 5309–5321 (2014).
3. C. Degueldre, H. Pleinert, P. Maguire, E. Lehman, J. Missimer, J. Hammer, K. Leenders, H. Böck, and D. Townsend, "Porosity and pathway determination in crystalline rock by positron emission tomography and neutron radiography," Earth Planet. Sci. Lett. **140**, 213–225 (1996).
4. B. Cagnoli and A. Piersanti, "Grain size and flow volume effects on granular flow mobility in numerical simulations: 3-D discrete element modeling of flows of angular rock fragments," J. Geophys. Res-Sol Ea **120**, 2350–2366 (2015).
5. S. Park, H. Cho, I. Yoon, and K. Min, "Measurement of droplet size distribution of gasoline direct injection spray by droplet generator and planar image technique," Meas. Sci. Technol. **13**, 859–864 (2002).
6. P. S. Prestes, D. D. Peres, A. Z. de Freitas, V. O. Consiglieri, T. M. Kaneko, M. V. R. Velasco, and A. R. Baby, "Particle size and morphological characterization of cosmetic emulsified systems by optical coherence tomography (OCT)," Braz. J. Pharm. Sci. **52**, 273–280 (2016).
7. J. M. Constantin, T. Godet, M. Jabaudon, J.-E. Bazin, and E. Futier, "Recruitment maneuvers in acute respiratory distress syndrome," Ann. Transl. Med. **5**, 290–290 (2017).
8. S. C. Mayo, A. W. Stevenson, and S. W. Wilkins, "In-line phase-contrast x-ray imaging and tomography for materials science," Materials **5**, 937–965 (2012).
9. D. M. Cooper, C. E. Kawalilak, K. Harrison, B. D. Johnston, and J. D. Johnston, "Cortical bone porosity: What is it, why is it important, and how can we detect it?" Curr. Osteoporos. Rep. **14**, 187–198 (2016).
10. M. J. Kitchen, G. A. Buckley, A. F. T. Leong, R. P. Carnibella, A. Fouras, M. J. Wallace, and S. B. Hooper, "X-ray specks: low dose in vivo imaging of lung structure and function." Phys. Med. Biol. **60**, 7259–7276 (2015).
11. W. C. Conner, J. F. Cevallos-Candau, E. L. Weist, J. Pajares, S. Mendioroz, and A. Cortes, "Characterization of pore structure: porosimetry and sorption," Langmuir **2**, 151–154 (1986).

12. K. Sing, "The use of nitrogen adsorption for the characterisation of porous materials," Colloid Surf. A **187-188**, 3–9 (2001).
13. O. Šolcová, L. Matějová, and P. Schneider, "Pore-size distributions from nitrogen adsorption revisited: Models comparison with controlled-pore glasses," Appl. Catal. A Gen. **313**, 167–176 (2006).
14. P. Fratzl, "Small-angle scattering in materials science - A short review of applications in alloys, ceramics and composite materials," J. Appl. Crystallogr. **36**, 397–404 (2003).
15. J. Ilavsky, P. R. Jemian, A. J. Allen, F. Zhang, L. E. Levine, and G. G. Long, "Ultra-small-angle X-ray scattering at the Advanced Photon Source," J. Appl. Crystallogr. **42**, 469–479 (2009).
16. L. E. Levine and G. G. Long, "X-ray imaging with ultra-small-angle X-ray scattering as a contrast mechanism," J. Appl. Crystallogr. **37**, 757–765 (2004).
17. M. Toiya, J. Hettinga, and W. Losert, "3D Imaging of particle motion during penetrometer testing: From microscopic to macroscopic soil mechanics," Granul. Matter **9**, 323–329 (2007).
18. J. A. Dijksman, N. Brodu, and R. P. Behringer, "Refractive index matched scanning and detection of soft particle," Rev. Sci. Instrum. **88**, 051807 (2017).
19. F. Guillard, B. Marks, and I. Einav, "Dynamic X-ray radiography reveals particle size and shape orientation fields during granular flow," Sci. Rep. **7**, 8155 (2017).
20. R. Cerbino, L. Peverini, M. A. C. Potenza, A. Robert, P. Bösecke, and M. Giglio, "X-ray-scattering information obtained from near-field speckle," Nat. Phys. **4**, 238–243 (2008).
21. R. P. Carnibella, M. J. Kitchen, and A. Fouras, "Determining particle size distributions from a single projection image." Opt. Express **20**, 15962–15968 (2012).
22. R. P. Carnibella, M. J. Kitchen, and A. Fouras, "Decoding the structure of granular and porous materials from speckled phase contrast X-ray images." Opt. Express **21**, 19153–19162 (2013).
23. A. F. T. Leong, D. M. Paganin, S. B. Hooper, M. L. Siew, and M. J. Kitchen, "Measurement of absolute regional lung air volumes from near-field x-ray speckles," Opt. Express **21**, 777–786 (2013).
24. L. D. Turner, B. B. Dhal, J. P. Hayes, A. P. Mancuso, K. A. Nugent, D. Paterson, R. E. Scholten, C. Q. Tran, and A. G. Peele, "X-ray phase imaging: Demonstration of extended conditions for homogeneous objects," Opt. Express **12**, 2960–2965 (2004).
25. A. Lipson, S. G. Lipson, and H. Lipson, *Optical Physics* (Cambridge University Press, 2010).
26. M. Sanchez del Rio and R. J. Dejus, "XOP v2.4 : Recent developments of the X-ray optics software toolkit," Proc. SPIE **8141**, 814115 (2011).
27. M. Matsumoto and T. Nishimura, "Mersenne twister: A 623-dimensionally equidistributed uniform pseudo-random number generator," ACM Trans. Model. Comput. Simul. **8**, 3–30 (1998).
28. K. Shoemake, "Uniform random rotations," in *Graphics Gems III,* D. Kirk, ed. (Academic Press, 1992), pp. 124–132.
29. D. Paganin, *Coherent X-Ray Optics* (Oxford University Press, 2006).
30. D. Paganin, S. C. Mayo, T. E. Gureyev, P. R. Miller, and S. W. Wilkins, "Simultaneous phase and amplitude extraction from a single defocused image of a homogeneous object." J. Microsc. **206**, 33–40 (2002).
31. R. Marks II, *Handbook of Fourier Analysis & Its Applications* (Oxford University Press, 2008).
32. M. M. Hall Jnr, V. G. Veeraraghavan, H. Rubin, and P. G. Winchell, "The approximation of symmetric x-ray peaks by Pearson type VII distributions," J. Appl. Crystallogr. **10**, 66–68 (1977).
33. W. H. Press, S. A. Teukolsky, W. T. Vetterling, and B. P. Flannery, *Numerical Recipes in C: The Art of Scientific Computing* (Cambridge University Press, 1988).
34. A. F. T. Leong, G. A. Buckley, D. M. Paganin, S. B. Hooper, M. J. Wallace, and M. J. Kitchen, "Real-time measurement of alveolar size and population using phase contrast x-ray imaging," Biomed. Opt. Express **5**, 4024–4038 (2014).
35. P. Churcher, P. French, J. Shaw, and L. Schramm, "Rock properties of Berea sandstone, Baker Dolomite, and Indiana limestone," in *SPE International Symposium on Oilfield Chemistry,* (Society of Petroleum Engineers, 1991).
36. A. Kingston and I. Svalbe, "Projective transforms on periodic discrete image arrays," in *Advances in Imaging and Electron Physics,* P. W. Hawkes, ed. (Elsevier Science, 2011), pp. 78–172.
37. P. Cloetens, M. Pateyron-Salomé, J. Y. Buffiére, G. Peix, J. Baruchel, F. Peyrin, and M. Schlenker, "Observation of microstructure and damage in materials by phase sensitive radiography and tomography," J. Appl. Phys. **81**, 5878 (1997).
38. J. Q. Shi, Z. Xue, and S. Durucan, "Supercritical CO2 core flooding and imbibition in Berea sandstone - CT imaging and numerical simulation," Energy Procedia **4**, 5001–5008 (2011).
39. K. Heim, F. Bernier, R. Pelletier, and L. P. Lefebvre, "High resolution pore size analysis in metallic powders by X-ray tomography," Case Stud. Nondestruct. Test. Eval. **6**, 45–52 (2016).
40. L. Thwala, "Protamine nanocapsules as carriers for oral peptide delivery," J. Control. Release **291**, 157–168 (2016).
41. Y. I. Nesterets and T. E. Gureyev, "Noise propagation in x-ray phase-contrast imaging and computed tomography," J. Phys. D. Appl. Phys. **47**, 105402 (2014).
42. M. J. Kitchen, D. M. Paganin, K. Uesugi, B. J. Allison, R. A. Lewis, S. B. Hooper, and K. M. Pavlov, "Phase contrast image segmentation using a Laue analyser crystal." Phys. Med. Biol. **56**, 515–534 (2011).
43. A. J. Carroll, G. A. Van Riessen, E. Balaur, I. P. Dolbnya, G. N. Tran, and A. G. Peele, "An iterative method for near-field Fresnel region polychromatic phase contrast imaging," J. Opt. **19** (2017).
44. C. T. I. Reviews, *Calculus, Single and Multivariable: Business, Mathematics* (Cram101, 2016).